Electrochimica Acta 476 (2024) 143680

Contents lists available at ScienceDirect

Electrochimica Acta

journal homepage: www.journals.elsevier.com/electrochimica-acta

Enhancing electrochemical N_2 reduction at mild conditions with Fe_xO_y co-deposited on amorphous MoS_2

Caio V.S. Almeida , Lucia H. Mascaro *

Department of Chemistry, Federal University of São Carlos, Rod. Washington Luiz, Km 235, São Carlos, SP CEP 13565-905, Brazil

ARTICLE INFO

Keywords:
Ammonia
Amorphous materials
Electrocatalyst
Gas diffusion layer
Nitrogen reduction reaction

ABSTRACT

Electrochemical reduction of N_2 can lead to the clean and sustainable production of NH_3 under environmental conditions. However, limited progress has been made as most catalysts lack efficient activity for N_2 fixation. Here, we report Fe_xO_y co-deposited on amorphous MoS_2 supported on a gas diffusion layer electrode (GDL) as an effective catalyst for N_2 reduction. The catalysts were prepared by electrodeposition, a simple and low-cost method. Physical characterizations revealed the amorphous nature of MoS_2 and while Fe_xO_y was evenly distributed over MoS_2. In 0.1 M Na_2SO_4, GDL/MoS_2-Fe-1 exhibited an NH_3 yield of 7.38 μmol h^{-1} cm^{-2}, a value almost 2 times greater than that obtained for MoS_2/GDL and a faradaic efficiency of 54.9 % at −0.2 V vs. reversible hydrogen electrode (RHE) at 25 °C. Also, the catalyst displayed high stability and durability, retaining almost 93 % of its original values after recycling tests. The amorphous MoS_2-Fe_xO_y provides new insight into designing efficient and robust catalysts for nitrogen reduction.

1. Introduction

The production of NH_3 is crucial for human development and the global economy, as ammonia is the second most synthesized chemical in the world [1,2]. In addition, ammonia is a promising carbon-free energy carrier with a high hydrogen content (17.6 % by mass), high energy density (4.25 kWh L^{-1}), and easy handling and transport [3,4].

Currently, the production of NH_3 on a world scale depends on the Harber-Bosch (H-B) process, developed in the early 20th century. However, to increase the reaction rate, the industrial synthesis of ammonia is carried out at high temperatures (400–600 °C) and pressures (20–40 MPa) [1,4]. Furthermore, the H-B process requires a pure H_2 precursor mainly derived from natural gas reform [5,6]. As a result, the annual synthesis of NH_3 consumes about 1–2 % of global electrical energy and is responsible for approximately 3 % of global CO_2 [7].

Thus, researchers have been developing technologies capable of using H_2O to replace H_2 as a source of protons to produce NH_3 at room temperature and atmospheric pressure [8]. An electrochemical approach to the nitrogen reduction reaction (NRR) to ammonia is a promising ecological and sustainable process to replace the Harber-Bosch process [8,9]. However, the high N≡N bond energy (940.95 kJ mol^{-1}) in competition with the strong hydrogen evolution reaction (HER) poses substantial obstacles to reaction kinetics and Faradaic efficiency (FE) in the NRR process [10,11]. In this regard, a great effort has been made to design low-priced, yet active and stable electrocatalysts to facilitate the NRR and restrain the undesired HER.

Mo and Fe are important elements in the enzyme nitrogenase due to the active site called iron-molybdenum cofactor (FeMoco), responsible for catalyzing N_2 fixation under environmental conditions in various biological systems [12]. Inspired by nature, several Fe-based [13–15] and Mo-based [16–18] catalysts have been employed for the electrochemical NRR. Among them, MoS_2 is a promising NRR candidate due to its tunable electronic structure and abundant edge active sites [16]. Nonetheless, the NRR performance of most existing MoS_2-based catalysts is still far less satisfactory due to their limited available edge sites and the competition from the HER, which mostly prevented effective electron transfer for the NRR [17].

The addition of co-catalysts has been considered an effective strategy for improving the electrocatalytic performance of MoS_2 materials. A theoretical study has shown that the Fe-deposited MoS_2 sheets exhibit higher selectivity for N_2 fixation due to the strong electron interaction between Fe and MoS_2 [19]. For example, Zhao et al. [12] reported Fe nanodot-decorated MoS_2 nanosheets on carbon cloth (Fe-MoS_2/CC) as a catalyst for NRR. The as-obtained material showed an average NH_3 yield of 12.5 μg h^{-1} cm^{-2} and a faradaic efficiency of 10.8 % at −0.1 V vs RHE, values 3.15 and 6.4 times higher, respectively, for the MoS_2/CC

* Corresponding author.
E-mail address: lmascaro@ufscar.br (L.H. Mascaro).

https://doi.org/10.1016/j.electacta.2023.143680
Received 7 August 2023; Received in revised form 13 November 2023; Accepted 16 December 2023
Available online 23 December 2023

electrode.

Besides, Fe oxide species (such as FeO and Fe_2O_3) can enhance the NRR due to their excellent redox property caused by the easy gain and loss of electrons in the d shell of the metal cations [20,21]. In this sense, Ma and co-workers [21] showed experimentally and theoretically, that Fe_2O_3 nanoparticles anchored on MoS_2 nanoflowers (Fe_2O_3@MoS_2) can enhance the NRR performance of MoS_2. According to DFT calculations, Fe_2O_3@MoS_2 is better able to activate N_2 molecules compared to MoS_2, as reflected by its lower energy barrier and greater charge transfer from active sites to N_2 molecules.

Amorphous materials have a nonperiodic structure of the internal arrangement of atoms or molecules. Their abundant defects in both surface and bulk as well as unique electronic properties make them promising candidates for electrochemical NRR [19]. Hence, increasing the concentration of edge layer sites of MoS_2 is another approach to enhance its NRR activity since the MoS_2 basal plane is inert for N_2 electroreduction [19].

An amorphous structure of MoS_2 presents a greater concentration of the edges layer sites compared to crystalline MoS_2 and, therefore, can provide abundant unsaturated coordination sites and surface-exposed defects, which provide active sites to capture and activate the N_2 molecule [22]. Moreover, amorphous materials are generally prepared at milder temperatures and with faster solidification processes than crystalline materials. The simple preparation methods, together with the low cost of the precursor materials, make this class of catalysts very attractive for the development of electrochemical and photo-electrochemical NH_3 production devices [23].

So far, the use of amorphous catalysts for the electrochemical reduction of N_2 is scarce in the literature. This work offers a promising opportunity to investigate amorphous MoS_2 for N_2 fixation. Thus, we report Fe_xO_y co-deposited on amorphous MoS_2 supported on a gas diffusion layer electrode (GDL) as an effective catalyst for the NRR. At 0.1 M Na_2SO_4, GDL/MoS_2-Fe-1 exhibited a remarkable NH_3 yield of 7.38 μmol h^{-1} cm^{-2}, a value almost 2 times greater than that obtained for MoS_2/GDL and a faradaic efficiency of 54.9 % at −0.2 V vs. RHE.

2. Experimental section

2.1. Chemicals

Ammonium tetrathiomolybdate ($[NH_4]_2MoS_4$ - 99.97 %), Sodium perchlorate ($NaClO_4$ - ≥ 98 %), Anhydrous sodium sulfate ($NaSO_4$ - ≥99.0 %), Iron (II) Chloride ($FeCl_2$ $4H_2O$ – 98 %), para–(dimethylamino) benzaldehyde (p–$C_9H_{11}NO$), ascorbic acid ($C_6H_8O_6$ – ≥ 99 %), ammonium chloride (NH_4Cl - 99.5 %), hydrazine hydrate (N_2H_4 80 % solution in H_2O), concentrated hydrochloric acid (HCl - 37 wt%) sulfuric acid (H_2SO_4 – 98 %), nitric acid (HNO_3 – 65 %) and phosphoric acid (H_3PO_4 – 85 % in H_2O) were purchased from Merck KGaA, Brazil. Ethanol (C_2H_5OH, 99.7 %) was purchased from Teda Inc. All reagents were of analytical grade and used without further purification. A gas diffusion layer (GDL – TGP-H-090 Wet proofed) was obtained from Toray Industries. Milli-Q ultrapure water (18.2 MΩ cm) was used in the preparation of all the solutions.

2.2. Pre-treatment of GDL

Before the deposition of the catalysts, the GDL substrate needed to be treated in acid to increase the hydrophilicity of the material, which is hydrophobic due to the presence of PTFE on its surface. For the acid treatment method, concentrated H_2SO_4/HNO_3 (V/V:3/1) solution were prepared. The GDL (0.5 × 0.5 cm) was dropped into the acid solution and subjected to an ultrasonic bath for 10 min at room temperature. Then, the substrate was rinsed copious times with ultrapure water and dried in the oven at 60 °C for 1 h.

2.3. Synthesis of amorphous MoS_2 (GDL/MoS_2)

The molybdenum sulfide film was prepared by electrodeposition technique according to the literature [24,25]. Chronoamperometries (CA) were performed in the potential of −1.1 V for 60 min using 4 mmol L^{-1} $(NH_4)_2MoS_4$ and 0.1 mol L^{-1} $NaClO_4$ as the precursor solution previously deaerated with N_2 for 15 min. The GDL substrates (0.25 cm^2) were used as the working electrode, while a Pt plate (1 cm^2) and Ag/AgCl/Cl^- (saturated with KCl) were the counter and reference electrodes, respectively.

2.4. Synthesis of amorphous MoS_2-Fe (GDL/MoS_2-Fe)

Fe was deposited over GDL/MoS_2 catalyst by electrodeposition. For this, a solution containing 50 mmol L^{-1} $FeCl_2$ $4H_2O$ and 10 mmol L^{-1} ascorbic acid at pH 3.5 (with the addition of 1.0 mol L^{-1} HCl) was used, previously deaerated with N_2 for 15 min. Electrodeposition was carried out at a constant potential of −1.0 V vs. Ag/AgCl/Cl^- (saturated with KCl) and the time deposition was varied thus: 60, 150 and 300 s. The Fe deposition times were chosen to control the atomic proportion of Fe/(Mo+*S*) between the catalysts so that the effects of small (60 s) and high (300 s) amounts of Fe deposited on the catalyst were evaluated.

The same system with three electrodes, described in the item above, was used in these depositions. The catalysts were named GDL/MoS_2-Fe-1, GDL/MoS_2-Fe-2 and GDL/MoS_2-Fe-3 according to the Fe deposition time, 60, 150 and 300 s, respectively. This nomenclature was used during the entire text.

2.5. Physical characterization

The crystalline structure was determined by X-ray diffraction (XRD) analysis performed using a BRUKER diffractometer model D8 ADVANCE, operating with Cu Ka radiation (k = 0.15406 nm). The diffraction patterns were registered every 2θ angles from 20 to 90°, with a scan rate of 2° min^{-1}. The crystallographic compositions of the catalysts through the X'Pert HighScore Plus program were compared with reference standards of the Joint Committee of Powder Diffraction Data Standards (JCPDS) database.

The morphology and film thickness were evaluated by dual-beam scanning electron microscopy (SEM) equipped with focused ion beam (FIB) observation equipment (FEI Vectra-IET). The composition of the films was studied by energy dispersive X-ray (EDX, FEI-XL30-FEG with Oxford Instruments-Link ISIS 300 detector). Laser Raman spectra were obtained using a Micro Raman Horiba iHR 550 spectrophotometer and a 532 nm laser.

The chemical surface analysis of the catalysts was realized by X-ray photoelectron spectroscopy (XPS) using a K-alpha XPS (Thermo Scientific) spectrometer with monochromatic Al Kα ($h\nu$ = 1486 eV) radiation as the excitation source. The binding energies (BE) were evaluated using the C 1 s spectrum (BE = 284.6 eV) as the reference. The spectra were fitted using CasaXPS (software version 2.3.15).

2.6. N_2 reduction reaction

The N_2 reduction reaction experiments were performed in an H-type electrocatalytic cell under ambient conditions. It consists of two cells separated by a Nafion™ membrane. The Nafion™ membrane was used as received, with no additional acid treatment. A counter electrode was placed in the anodic compartment, where the oxidation process generates protons. The reference electrode and working electrodes were placed in the cathodic compartment where the NRR takes place.

A potentiostat/galvanostat (Autolab Model PGSTAT 302 N) with a typical three electrode system was used to carry out all the electrochemical measurements. Herein, GDL/MoS_2, GDL/Fe and GDL/MoS_2-Fe were implemented as the working electrode, whereas a Pt plate (1 cm^2) and an Ag/AgCl/Cl^- (saturated with KCl) were implemented,

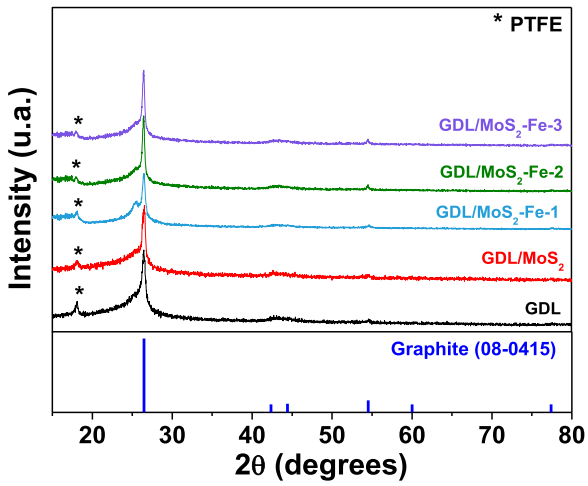

Fig. 1. X-ray diffraction patterns for GDL substrate, GDL/MoS_2 and GDL/MoS_2-Fe catalysts.

respectively, as counter and reference electrodes The potentials reported in the paper are expressed on the scale of the reversible hydrogen electrode (RHE) with the following equation: E (vs RHE) = E_{appl} (vs. Ag/AgCl/Cl^- $_{(sat.\ KCl)}$) + pH × 0.059 V + 0.197 V [26]. Subsequently, the current density was recorded with respect to the geometric surface area of the working electrode.

The reaction was carried out in 60 mL (25 mL in the anodic compartment and 35 mL in the cathodic compartment) of 0.1 mol L^{-1} Na_2SO_4 in which high purity N_2 gas (99.999 %, 20 mL min^{-1}) was bubbled for 45 min for complete saturation of the medium, as well as throughout the entire experiment (2 h). A 30 mL acid trap of 0.005 mol H_3PO_4 [27] was connected to the cathodic compartment for ammonia storage. The reactions were reproduced in triplicate.

2.7. NH_3 detection

The yield amount of NH_3 ($C[NH_3]_{N_2}$) in the solution was measured by a colorimetric indophenol blue method [28] using the Merck Spectroquant® commercial kit. Briefly, 5.0 mL aliquots were mixed with 0.6 mL of the NH4–1 reagent and a micro spoon of the NH4–2 reagent (as supplied in the kit), followed by stirring for 5 min and resting for 10 min for the complete reaction of the reagents. Then, 4 drops of the NH4–3 reagent were added to the aliquots followed by stirring for 5 min and standing for 20 min.

The prepared samples were then analyzed on a UV–vis Spectrometer (Varian, Cary 5 G UV–vis-NIR) at a wavelength of 690 nm. A calibration curve for NH_3 was constructed, using the procedure described above in triplicate, on standard NH_4Cl solutions prepared in 0.1 mol L^{-1} Na_2SO_4 media with NH_4^+ concentrations ranging from 0.00 to 3.00 μg mL^{-1}. A curve fit ($y = 0.2998x + 0.0096$, $R^2 = 0.99926$) of the three independent calibrations shows a good linear relationship between the absorbance value and the NH_3 concentration (Fig. S1).

To eliminate the possible exterior sources of contaminations [29] the corresponding Ar-saturated ($C[NH_3]_{Ar}$) condition and the open-circuit N_2-saturated condition ($C[NH_3]_{Open}$) for the NRR experiment were used as the baseline for NH_3 production. Thus, the corrected $C[NH_3]$ produced during the N_2 reduction was calculated using the following equation (Eq. (1)):

$$C[NH_3] = C[NH_3]_{N_2} - C[NH_3]_{Ar} - C[NH_3]_{Open} \quad (1)$$

The NH_3 yield rate was determined by (Eq. (2)):

$$NH_3 \text{ yield rate } \left(\text{mol } h^{-1}\ cm^{-2}\right) = (C[NH_3] \times V)/(t \times A) \quad (2)$$

Where $C[NH_3]$ is the corrected concentration of NH_3 production (mol L^{-1}); V is the volume of the electrolyte (L); A is the geometric surface area of the working electrode (cm^2), and t is the electrolysis reaction time (h).

The faradaic efficiency (FE) can be calculated using the following equation (Eq. (3)):

$$FE = (3F \times C[NH_3] \times V)/Q \quad (3)$$

Where F refers to the Faraday constant (96,485.3 C mol^{-1}), Q is the quantity of electric charge via the applied potential during the entire experiment (C).

2.8. N_2H_4 detection

The Watt and Chrisp method was adopted to quantify the N_2H_4 in the electrolyte after the reaction [30]. The coloring agent was prepared by mixing 6.0 g of p-$C_9H_{11}NO$ with 30 mL of concentrated HCl and 300 mL of C_2H_5OH. Then, 5 mL of the electrolyte was taken from the acid trap and mixed with 5 mL of the coloring agent followed by stirring for 10 min and standing for 20 min. The absorbance of the solution was constructed using standard hydrazine hydrate solutions ranging from 0.2 to 1.2 μg mL^{-1}. As demonstrated in Fig.S2, a good linear relationship ($y = 0.7184x + 0.2456$, $R^2 = 0.99939$) between the absorbance value and the N_2H_4 concentration were obtained in three independent calibrations.

2.9. FTIR measurements

In situ FTIR measurements were carried out by using a Nicolet 6700 FTIR spectrometer (Thermo Fisher) equipped with MCT (Mercury-Cadmium- Telluride) detector cooled with liquid nitrogen. Spectra were computed from an average of 64 interferograms. The spectral resolution was set to 4 cm^{-1}. The electrochemical infrared cell was fitted with a CaF_2 prismatic window. The catalyst was electrodeposited on a glassy carbon electrode (7 mm in diameter) previously polished to a mirror finish (alumina, 0.05 μm) to obtain good reflectivity. The reaction was carried out in 0.1 mol L^{-1} Na_2SO_4 in which high purity N_2 gas was bubbled for 45 min for complete saturation of the medium. The spectra were collected during chronoamperometry at −0.2 V vs RHE for 1000s.

3. Results and discussion

3.1. Physical characterization

XRD analyzes were performed to identify the crystallographic structure of the GDL substrate and as-synthesized GDL/MoS_2 and GDL/MoS_2-Fe catalysts. According to Fig. 1, the diffraction peaks at 26.4, 42.3, 44.5 and 54.6° corresponds to (002), (100), (101) and (004) planes of the GDL substrate (PDF No. 00–041–1487) [31].The other peak located at 18.1° relates to PTFE (PDF No. 00–045–1594) [32].

On the other hand, no peaks for the molybdenum sulfide were detected. The absence of these characteristic diffraction peaks suggests the existence of MoS_2 in the amorphous phase, which is consistent with previous reports for MoS_2 prepared by electrodeposition [24,25]. In addition, the XRD patterns showed that for all the GDL/MoS_2-Fe catalysts, no crystalline Fe or oxidized species peaks could be observed, indicating the amorphous nature of the Fe electrodeposited.

The morphology and chemical components of the catalysts are characterized by SEM/EDX, as illustrated in Fig. 2. SEM images for the GDL/MoS_2 (Fig. S3a–S3c) catalyst were taken at different magnifications and showed a globular form, typically for amorphous MoS_2 films, consistent with the XRD data (Fig. 1) [25,33].

Fig. 2a–2c illustrates the SEM images at different magnifications for GDL/MoS_2-Fe-1. The Fe deposit (Fig. 2b) consists of a sheet-like structure. In contrast, the electrodeposition of Fe did not induce morphological changes in the MoS_2 film (Fig. 2c), with the typical globular form still observed.

However, increasing the Fe deposition time, the films become rough,

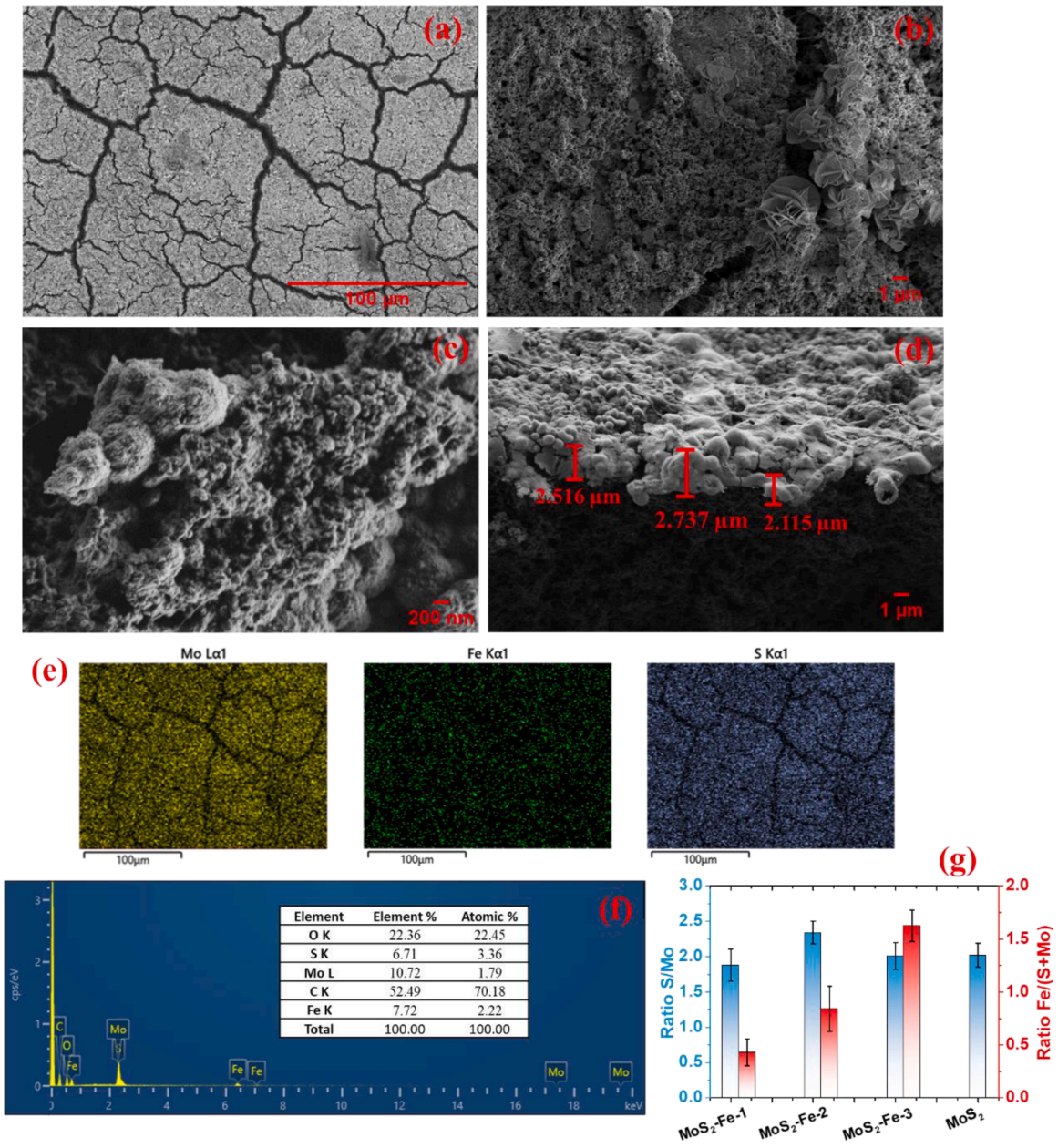

Fig. 2. (a, c) SEM images at different magnifications for GDL/MoS_2-Fe-1. (d) GDL/MoS_2-Fe-1 film thickness. Image obtained by a SEM equipped FEG observation equipment. (e) EDX elemental mapping distribution and (f) EDX spectrum with 500x magnification. (g) Elemental atomic ratio obtained by EDX.

and the sheet-like structure is more abundant, as observed in SEM images for GDL/MoS_2-Fe-2 (Fig. S4a–S4c) and GDL/MoS_2-Fe-3 (Fig. S5a–S5c) catalysts, indicating the successful deposition of Fe onto the MoS_2 films. Fig. 2d shows the results of the thickness value for three different regions of GDL/MoS_2-Fe-1 film. The mean thickness of GDL/MoS_2-Fe-1 film is about 2.44 ± 0.315 µm.

The presence of S, Mo, and Fe elements in the GDL/MoS_2-Fe-1 film is observed from the EDX mappings in Fig. 2e, 2f. The same is observed in EDX mappings for GDL/MoS_2 (Fig. S3d), GDL/MoS_2-Fe-2 (Fig. S4d) and GDL/MoS_2-Fe-3 (Fig. S5d), demonstrating that the elements are evenly dispersed in the substrate.

EDX spectroscopy was performed to evaluate the atomic ratio of S/Mo and Fe/(*S*+Mo) in the catalysts (Figs. 2g and S6). Fig. 2g shows that the atomic ratio of S/Mo ranged between 1.88 and 2.34 and it was assumed that MoS_2 species were deposited [24,25,34,35]. The Fe/(*S*+Mo) atomic ratios show that the amount of Fe deposited grows continuously as the time of deposition increases. In addition, for all catalysts, the stoichiometry between S/Mo was not lost with Fe deposition.

To further confirm the amorphous nature of the as-prepared catalysts, Raman scattering spectra are recorded and shown in Fig. S7. Spectra of GDL (Fig. S7a) presented a band at 734 cm^{-1} attributed to C-F symmetric stretching mode in PTFE. Besides, another band originated from the overlapping of two bands located at 1380 and 1572 cm^{-1} are related to the stretching of the C–C bond and the in-plane hexagonal vibrations of C–C in a graphitic structure [36].

For GDL/MoS_2 and GDL/MoS_2-Fe-1 catalysts (Fig. S7b), Raman spectra revealed a poor definition of the characteristic peaks expected for crystalline MoS_2 [34,35], which suggests that crystalline MoS_2 is not present in significant quantities in the as-deposited catalyst and an amorphous MoS_2 and MoS_2-Fe films were deposited.

The Raman spectrum analysis agrees with the XRD and SEM data, revealing the amorphous nature of the materials. GDL/MoS_2 exhibited two broad brands at 321 and 417 cm^{-1}, ascribed to the in-plane Mo-S

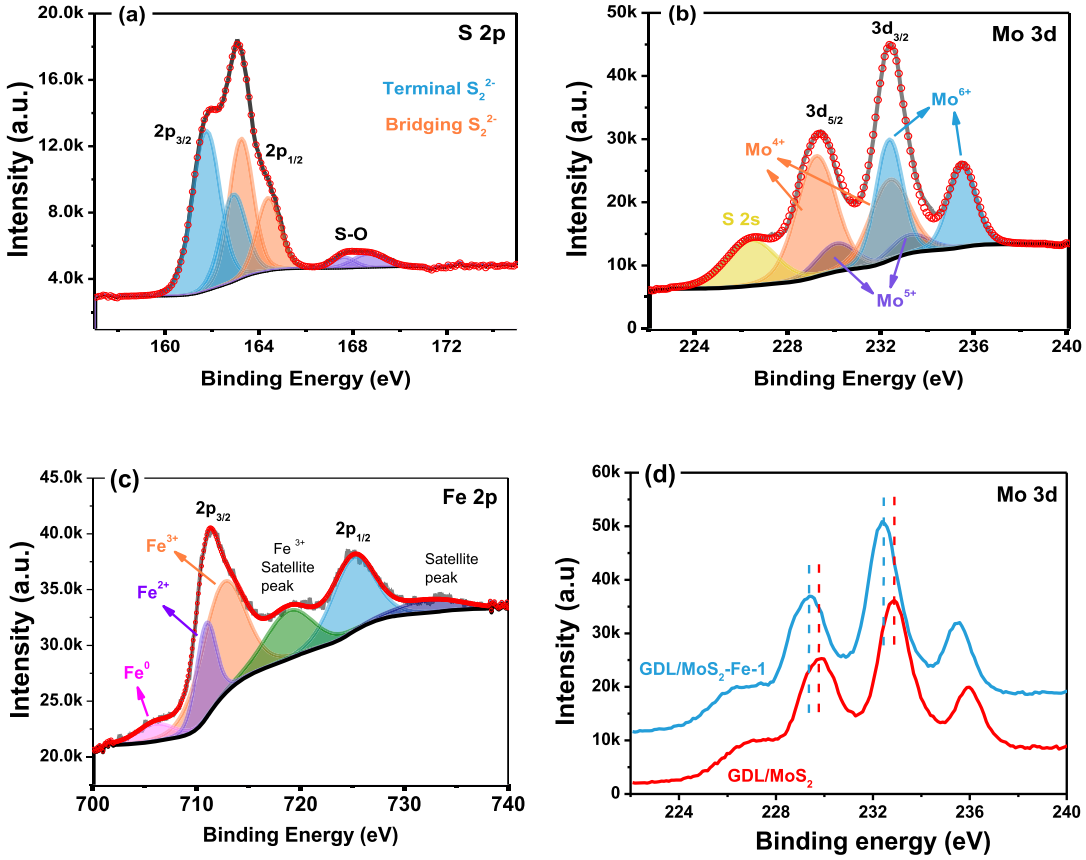

Fig. 3. High-resolution spectra of (a) Mo 3d, (b) S 2p and (c) Fe 2p of GDL/MoS_2-Fe-1. (d) Displacement of the Mo 3d binding energies for GDL/MoS_2-Fe-1 compared to GDL/MoS_2.

mode (E^1_{2g}) and the out-plane Mo-S mode (A_{1g}), respectively [34–37]. A broad band located at 800–900 cm^{-1} can be ascribed to MoO_3 was observed in all catalysts [38].

For GDL/MoS_2-Fe-1 catalyst (Fig. S7b), another two bands appear at 211 and 274 cm^{-1} that can be attached to α-Fe_2O_3, indicating that Fe is presented in the oxidized form [39,40]. Compared with those of GDL/MoS_2, the vibrational bands of GDL/MoS_2-Fe all showed displacement to lower values, indicating a chemical change in the Mo–S bond due to the electronic interaction between MoS_2 and Fe [12].

X-ray photoelectron spectroscopy (XPS) was used to verify the surface chemical composition and valence state of the S, Fe and Mo atoms on the MoS_2 and MoS_2-Fe catalysts. Fig. 3a shows the survey XPS spectra for GDL/MoS_2 and GDL/MoS_2-Fe catalysts. As expected, the survey scan spectrum (Fig. S8a) confirmed the presence of S, Fe, Mo, C, F and O elements in the catalysts.

According to Table S1, the S/Mo ratio for the MoS_2/GDL film was 1.92/1, while for the MoS_2-Fe-1 the S/Mo/Fe ratio was 2.11/1/0.42, which is very close to the stoichiometric MoS_2, and agrees with the EDX spectroscopy (Fig. 2f).

The high-resolution XPS data in the S 2p region for GDL/MoS_2-Fe-1 (Fig. 3a) and GDL/MoS_2 (Fig. S8b) are composed of terminal S_2^{2-} and bridge S_2^{2-} configurations each with two doublets [41]. The atomic percentages for the terminal S_2^{2-} and bridge S_2^{2-} configurations for GDL/MoS_2 (Table S2) were 48.4 % and 40.4 %, respectively. One more doublet related to sulfate (S-O) was identified in both catalysts.

However, after Fe deposition, there is a slight increase in the terminal S configuration to 53.7 %, indicating greater exposure of the lateral sites of the MoS_2-Fe-1 catalyst [41–43]. As discussed before, the basal surface of MoS_2 is inert, although the edge of MoS_2 catalyst is active for N_2 electroreduction [19,20]. Thus, it is reasonable to assume that Fe deposition can enhance GDL/MoS_2-Fe catalytic activity and facilitate N_2 adsorption due to increasing the concentration of edge layer sites of MoS_2.

The molybdenum region for GDL/MoS_2-Fe-1 (Fig. 3b) and GDL/MoS_2 (Fig. S8c) was deconvolved into three doublets (Mo $3d_{5/2}$ and $3d_{3/2}$) equivalent to the Mo^{4+}, Mo^{5+} and Mo^{6+} states [24,44]. The Mo 3d spectrum contains peaks due to Mo^{6+} due to molybdenum oxysulfide, indicating the oxide formation during the synthesis or film oxidation during the storage. However, OH^- is produced during cathodic deposition (Eq. (4)), which may facilitate the formation of this species [45]. Another peak is shown at 226.4 eV, which was attributed to S 2 s [42].

$$[MoS_4]^{2-} + 2H_2O + 2e^- \rightarrow MoS_2 + 2HS^- + 2OH^- \quad (4)$$

For GDL/MoS_2-Fe-1, the binding energies of Mo $3d_{5/2}$ and Mo $3d_{3/2}$ show a negative shift after Fe deposition, as displayed in Fig. 3d. The electronic structure is directly related to the binding energy [12]. So, the binding energy displacement in the Mo XPS spectra suggests the electronic interaction between Fe and MoS_2. Likewise, the binding energies of S $2p_{3/2}$ and S $2p_{1/2}$ for GDL/MoS_2-Fe-1 also show a negative shift compared with those for GDL/MoS_2, as shown in Fig. S8c.

3.2. NRR on GDL/MoS_2 and GDL/MoS_2-Fe catalysts

To investigate the catalytic activity of GDL/MoS_2 and GDL/MoS_2-Fe catalysts towards NRR, electrochemical experiments were conducted in N_2-saturated 0.1 mol L^{-1} Na_2SO_4. The NRR was performed in the neutral electrolyte Na_2SO_4 to reduce the competitive H^+ adsorption in HER.

Fig. 4a shows the LSV curves at a scan rate of 10 mV s^{-1} to determine the electrochemical window for the NRR over the materials. For all catalysts, there is an increase in the current density after the electrolyte

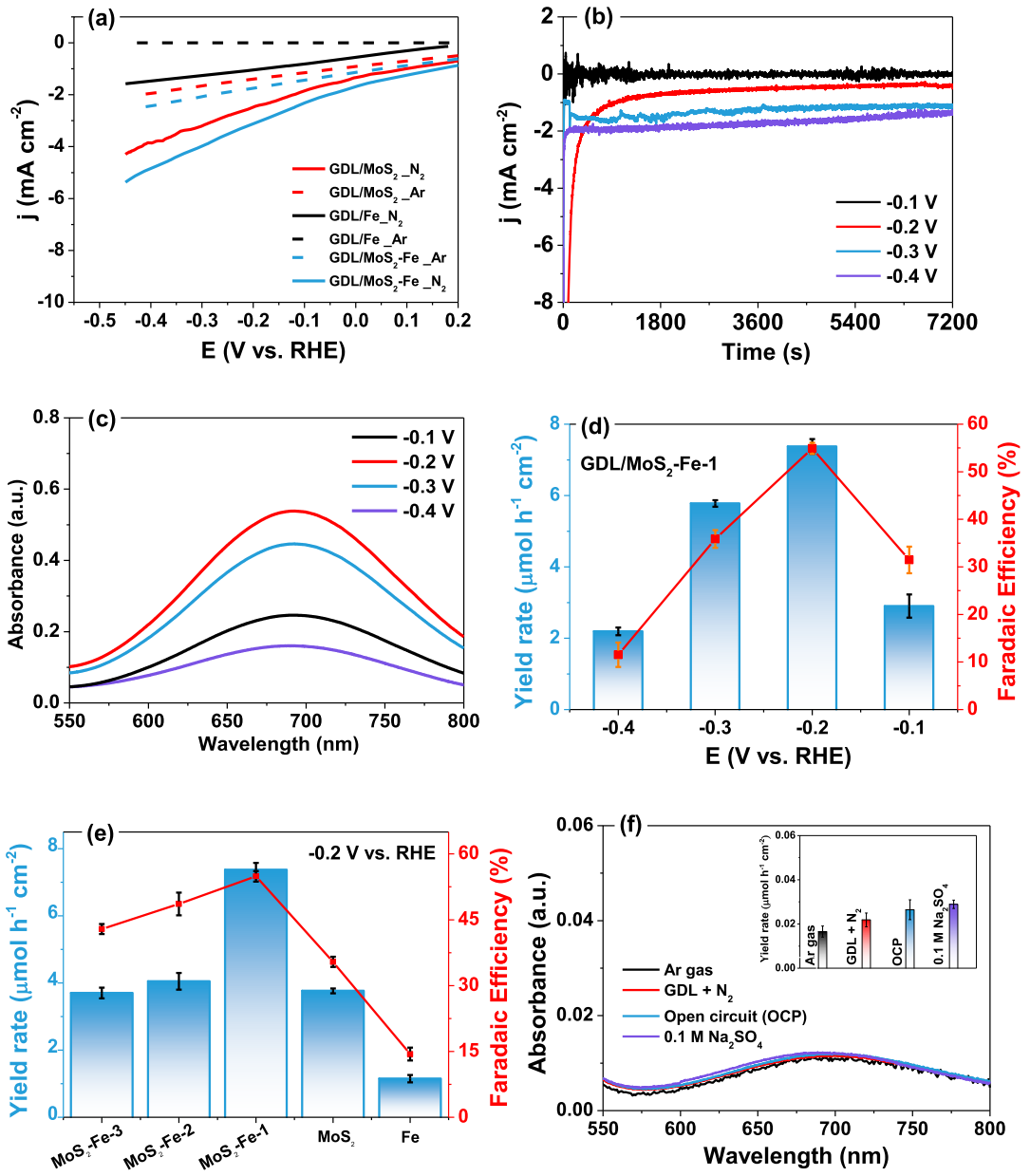

Fig. 4. (a) LSV curves of GDL/MoS_2, GDL/Fe and GDL/MoS_2-Fe-1 in 0.1 mol L^{-1} Na_2SO_4 electrolyte saturated with N_2 and Ar. (b) Time-dependent current density curves of GDL/MoS_2-Fe-1 for NRR at different potentials (c) UV–vis absorption spectra stained with indophenol indicator at different potentials of GDL/MoS_2-Fe-1 (d) NH_3 yield rates and FE at different potentials of GDL/MoS_2-Fe-1. (e) NH_3 yield rates and FE for GDL/MoS_2-Fe with different Fe deposition times, GDL/Fe and GDL/MoS_2 catalysts at −0.20 V vs. RHE. (f) UV–vis absorption spectra of the electrolytes stained with indophenol indicator at −0.20 V for 2 h under various conditions. The insert: NH_3 yield rates under various conditions.

has been purged with N_2, indicating the occurrence of the NRR.

The time-dependent current density curves of the GDL/MoS_2-Fe-1 catalyst at different potentials are shown in Fig. 4b, and 4c is relevant UV–vis absorption spectra of the electrolytes colored with the indophenol indicator at different potentials for 2 h. As shown in Fig. 4d, the NH_3 yield rates and FE initially increase as the electrolysis potential becomes more negative. However, as the potential moves below −0.2 V vs. RHE, the NH_3 yield rates and FE decrease rapidly, which might result from the competitive HER [12,46].

At −0.20 V vs. RHE, GDL/MoS_2-Fe-1 presents the highest NH_3 average yield rate of 7.38 μmol h^{-1} cm^{-2}, a value almost 2 times greater than that obtained for GDL/MoS_2, and a corresponding FE of 54.9 %. A previous study has demonstrated that oxidized Fe species can improve water attraction and acts as a proton channel to promote N_2 reduction, which can enhance the MoS_2 activity [20,47]. Besides, the Fe center can transfer electronic charges to MoS_2, facilitating N_2 molecular adsorption and activation [17].

The possible N_2H_4 production was detected by Watt and Chrisp method (Fig. S9a), but no detectable N_2H_4 was observed for all catalysts at different potentials (Fig. S9b–9e). The result rules out the formation of hydrazine and signifies the formation of NH_3 only, indicating that the catalysts are selective for ammonia production.

To investigate the effect of Fe deposition on MoS_2 NRR, several GDL/MoS_2-Fe, varying the Fe deposition time, were tested toward NRR. GDL/Fe was also synthesized to explore the effect between Fe and MoS_2. The NRR performances of GDL/Fe after 2 h of potentiostatic electrolysis at different potentials are presented in Fig. S10a.

As shown in Fig. 4e, when the atomic ratio of Fe/(Mo+*S*) changed

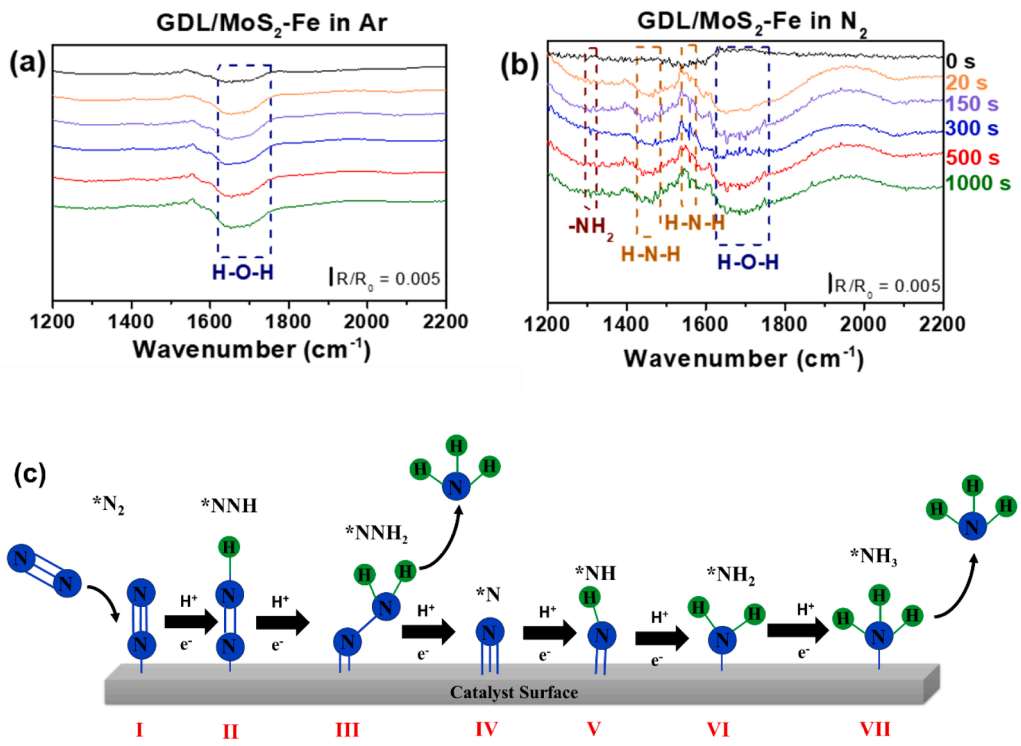

Fig. 5. Electrochemical *in situ* FTIR spectra of the NRR on the GDL/MoS_2-Fe-1 catalysts at −0.2 V vs RHE in (a) Ar and (b) N_2. (c) Proposed NRR via an associative mechanism.

Table 1
A summary of the representative experimental studies on NRR using various electrocatalytic catalysts.

Catalyst	Electrolyte	Potential (V) vs. RHE	Detection method	NH_3 yield	Faradaic Efficiency (%)	Refs.
GDL/MoS_2-Fe-1	0.1 M Na_2SO_4	−0.2	Indophenol blue	2.07×10^{-9} mol s^{-1} cm^{-2} (127.17 μg h^{-1} cm^{-2})	54.9	This study
MoS_2@Fe(OH)$_3$	0.1 M Na_2SO_4	−0.45	Indophenol blue	4.23×10^{-10} mol s^{-1} cm^{-2}	2.76	[20]
1D-$MoS_{2-x}O_y$	0.1 M HCl	−0.35	Indophenol blue	5.56×10^{-8} mol s^{-1} cm^{-2}	9.86	[55]
PAL-MoS_2	0.1 M HCl	−0.1	Indophenol blue	1.98 μg h^{-1} cm^{-2}	44.36	[56]
1T-MoS_2–Ni	0.25 M $LiClO_4$	−0.3	Indophenol blue	63 μg h^{-1} cm^{-2}	27.66	[45]
Fe-MoS_2/CC	0.1 M KOH	−0.1	Indophenol blue	12.5 μg h^{-1} cm^{-2}	10.8	[12]
Ru/2H-MoS_2	0.01 M HCl	−0.15	Indophenol blue	0.91×10^{-10} mol s^{-1} cm^{-2} (5.6 μg h^{-1} cm^{-2})	12.2	[57]
Fe-MoS_2	0.1 M KCl	−0.2	ion chromatography	97.5 ± 6 μg h^{-1} cm^{-2}	31.6 ± 2	[58]
Mo SAs-Mo_2C/NCNTs	5 mM H_2SO_4 + 0.1 M K_2SO_4	−0.25	ion chromatography and Indophenol blue	16.1 μg h^{-1} cm^{-2}	7.1	[59]

from 0.43 (GDL/MoS_2-Fe-1) to 0.84 (GDL/MoS_2-Fe-2), the NH_3 yield rates and FE decreased sharply. At a higher Fe/(Mo+*S*) atomic ratio (1.64) for GDL/MoS_2-Fe-3, considering the standard deviation, the NH_3 yield rates and FE do not modify significantly. The NRR performances and the UV–vis absorption spectra of GDL/MoS_2-Fe-2 and GDL/MoS_2-Fe-3 after 2 h of potentiostatic electrolysis at different potentials are presented in Fig. S10c, S10d and Fig. S10e, S10f, respectively.

Additionally, GDL/Fe yields only a small amount of NH_3 and low FE compared to GDL/MoS_2 (Fig. S10g, S10h), which excludes the possibility that Fe/Fe_xO_y contributes as the leading active site for NRR in the GDL/MoS_2-Fe catalyst. The results show that the improved NRR activity in the GDL/MoS_2-Fe-1 catalyst originates from the synergistic effect between Fe and MoS_2. However, higher concentrations of Fe/Fe_xO_y may cover MoS_2 film and therefore block its active sites, which explains the decrease in NRR performance at higher Fe/(Mo+*S*) atomic ratios.

Next, several control experiments were performed, including: (i) bubbling Ar gas for 2 h applying a potential of −0.2 V vs. RHE using the MoS_2-Fe-1 catalyst as the working electrode; (ii) N_2 gas was bubbled into the cell in an open circuit (OCP) for 2 h; (iii) the GDL electrode without the MoS_2-Fe-1 catalyst, (iv) only 0.1 M Na_2SO_4 electrolyte without Ar/N_2 gas or applied voltage and (v) N_2 steam treated with oxidizing trapper (alkaline $KMnO_4$) and acid trapper (1 mM H_2SO_4).

As can be seen in Fig. 4f, when either Ar gas was used instead of N_2 gas or the catalyst-free GDL electrode was used, a negligible amount of NH_3 was detected. Insignificant amounts of NH_3 were detected at the OCP and in the 0.1 M Na_2SO_4 electrolyte. Similarly, there is no significant difference in the absorbance values of the electrolyte purged with N_2 with and without treatment (Fig. S11), indicating low contamination of the supplied gas. This is corroborated by the spectra for NO_x determination in N_2-saturated 0.1 M Na_2SO_4 (Figs. S12 and S13). These results suggest that NH_3 was produced by N_2 reduction in the presence of the GDL/MoS_2-Fe catalysts rather than the sources of contamination.

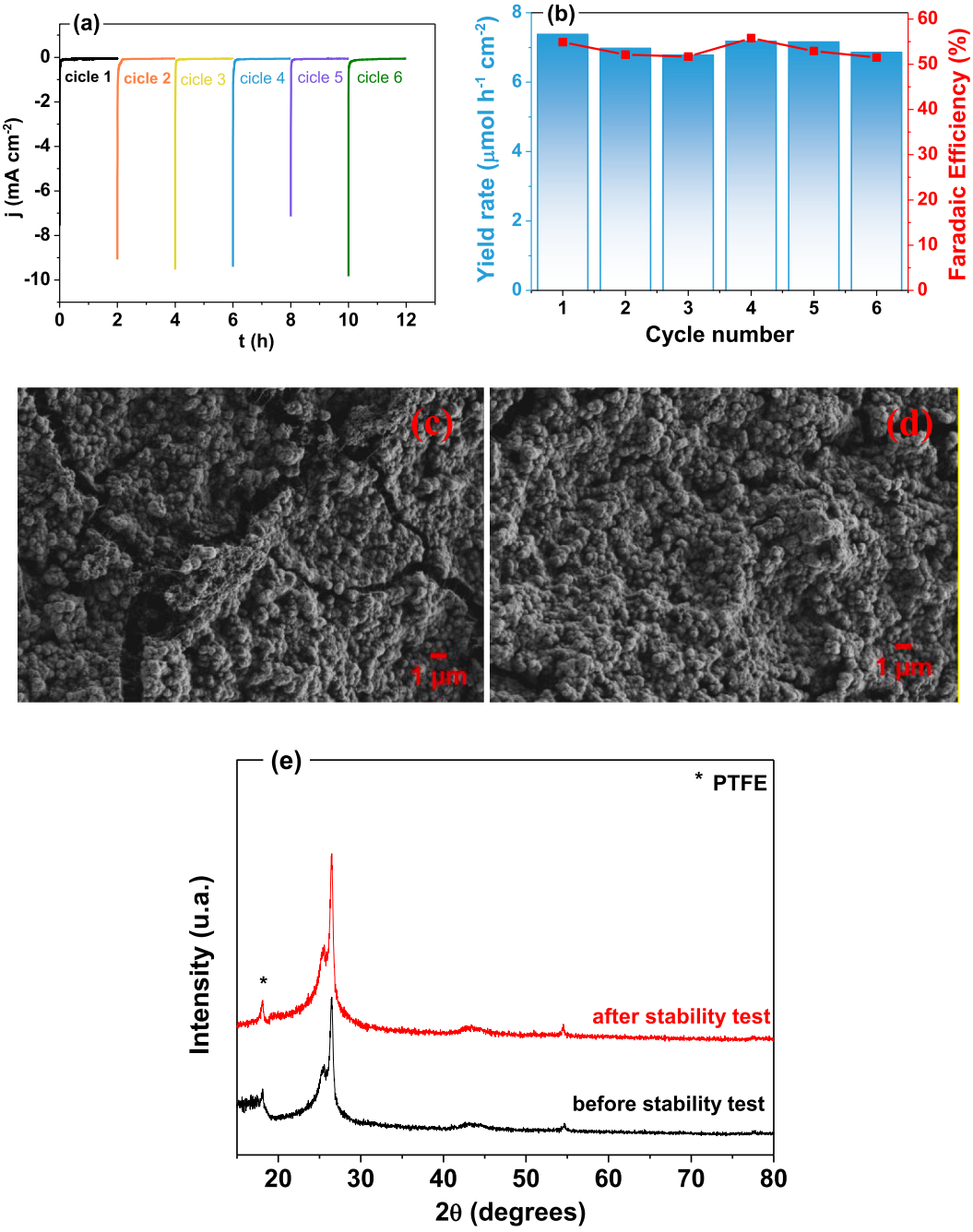

Fig. 6. (a) time-dependent current density curve at −0.2 V for GDL/MoS_2-Fe-1 in different cycles of NRR. (b) NH_3 yields and FEs for GDL/MoS_2-Fe-1 with recycling test at −0.2 V vs. RHE. SEM images before (c) and after (d) the cycling stability test. (e) X-ray diffraction patterns for GDL/MoS_2-Fe-1 catalyst before and after cycling stability test.

The influence of N_2 flow rate on electrocatalytic NRR was also investigated. Figure S14 shows that FE and NH_3 yield rates are unaffected when the N_2 flow rate increases from 20 to 60 mL min^{-1}. This result suggests that the rate reduction is impartial to the gas-solid interface. Moreover, since the speed of the electrocatalytic reaction is independent of N_2 concentration, the diffusion of N_2 is not the decisive step of the reaction.

In situ electrochemical FTIR experiments are also conducted to elucidate the reaction mechanism of the NRR over the GDL/MoS_2-Fe-1 at −0.2 V vs RHE in 0.1 M Na_2SO_4 solution (Fig. 5).

Different from the spectra in Ar (Fig. 5a), the spectra in N_2 for GDL/MoS_2 (Fig. 5b) have three extra negative-going peaks located at 1311, 1455 and 1560 cm^{-1}, which are assigned to H–N–H wagging, –NH_2 wagging and H–N–H bending, respectively, with the peak intensity increasing with increasing reaction time [48–50]. This result suggests the N≡N triple bond is cleaved into a single bond within the catalyst/electrolyte interface with the formation of –NH_x intermediate on the surface of GDL/MoS_2-Fe during the NRR.

Thus, based on the FTIR data and supported by several DFT studies [12,21,47,51–53] a possible mechanism was proposed (Fig. 5c), suggesting that ammonia synthesis follows the associative mechanism. In depth, N_2 is firstly adsorbed on the surface of the catalysts (I), and then a proton is attached to N_2 to form a *NNH bond (II), which initially activates cleavage of N≡N bond.

In the subsequent step, the further hydrogenation process can undergo the formation of *NNH_2, following a distal pathway or via an

alternative pathway with the formation of *NHNH. However, Ma et al. [21] founded that the ΔG values on Fe_2O_3@MoS_2 for the formation of *NNH_2 species are lower than *NHNH, indicating that associative distal mechanism is the favorable pathway for (III). In addition, no absorption of N_2H_4, an intermediate in the alternating route of NRR has been detected in the UV/Vis spectra of the catalysts (Fig. S9), suggesting the NRR reaction also occurred in our GDL/MoS_2-Fe_xO_y catalyst by the distal route mechanism [53].

After the first NH_3 desorption, the remaining nitrogen atom is negatively charged, as is beneficial for the approaching of the next H atom and further nitrogen reduction (IV). Finally, the continuous electron transfer and hydrogenation (V-VII), the formation and desorption of ammonia occur on the surface of the GDL/MoS_2-Fe-1 catalyst (VI).

Finally, the produced NH_3 can be easily dissolved in water, which is helpful for the release of NH_3 from the catalyst's surface, and the recovered active site can catalyze the next reaction cycle [52]. Therefore, the addition of Fe_xO_y to MoS_2 is an efficient strategy for enhancing NRR activity.

Table 1 summarizes the results from this study with previous data on NH_3 production and FE from the literature focused on MoS_2 electrocatalysts. Direct comparison of the results from different research groups is avoided because of the difference in experimental conditions and the absence of a self-consistent set of metrics for the NH_3 yield rates.

Nevertheless, the NH_3 yields and FE in the present study are positive, indicating that the amorphous nature of MoS_2 with a higher number of defects inducing more active site for N_2 fixation [54] combined with Fe_xO_y acting as an H^+ channel as a promising catalyst for NH_3 production.

Stability is another key criterion for evaluating catalyst performance. To prove the stability of the catalyst, GDL/MoS_2-Fe-1 was submitted to consecutive recycling electrolysis at −0.2 V vs. RHE (Fig. 6). Fig. 6a shows the time-dependent current density curves for GDL/MoS_2-Fe-1 in 6 cycles of NRR. As observed, the current density is not significantly reduced. The corresponding NH_3 yield rates and FE (Fig. 6b) retain almost 93 % of their original values, suggesting that the GDL/MoS_2-Fe-1 catalyst exhibits high stability and repeatable NRR performance during the recycling test.

After the recycling test, the SEM images (Fig. 6c, 6d) show that the structure and surface morphology of GDL/MoS_2-Fe-1 hardly changed after recycling testing, and XRD analysis (Fig. 6e) confirms that GDL/MoS_2-Fe-1 retains its amorphous structure. The EDX mapping (Fig. S15a–S15c) suggests that the Fe/Fe_xO_y species are uniformly dispersed on MoS_2. Also, the atomic ratio of S/Mo and Fe/(Mo+*S*) is calculated to be 1.92 and 0.43 (Fig. S15d), respectively, demonstrating no dissolution of Fe or MoS_2 species in the electrolysis process.

4. Conclusions

In summary, amorphous MoS_2-Fe_xO_y catalysts supported by GDL substrate were successfully synthesized via a simple and low-cost electrodeposition method and tested for electrochemical N_2 reduction under ambient conditions.

Physical characterization revealed the amorphous nature of the catalysts. Besides, their chemical state indicated the stoichiometric MoS_2 and oxidized Fe species. Different compositions of GDL/MoS_2-Fe were tested. However, the GDL/MoS_2-Fe-1, with the lowest Fe content, was the more active catalyst for NH_3 production, attaining 7.38 μmol h^{-1} cm^{-2} and a corresponding Faradaic efficiency of 54.9 % at −0.2 V vs. RHE in 0.1 M Na_2SO_4, values almost 2 times higher than GDL/MoS_2 catalyst. The amorphous structure of MoS_2 can provide a higher number of active sites, while Fe_xO_y can affect the electronic structure of MoS_2, facilitating N_2 adsorption and acting as an H^+ channel to promote NRR. In addition, the catalyst displayed high stability and durability, retaining almost 93 % of its original values after recycling tests.

This study not only provides an exciting earth-abundant catalyst for NH_3 production at mild conditions but also opens up a promising opportunity to synthesize amorphous materials for N_2 fixation.

CRediT authorship contribution statement

Caio V.S. Almeida: Conceptualization, Investigation, Methodology, Formal analysis, Data curation, Funding acquisition, Writing – original draft. **Lucia H. Mascaro:** Supervision, Conceptualization, Funding acquisition, Writing – review & editing.

Declaration of Competing Interest

The authors declare that they have no known competing financial interests or personal relationships that could have appeared to influence the work reported in this paper.

Data availability

Data will be made available on request.

Acknowledgments

This research was funded by Fundação de Amparo a Pesquisa do Estado de São Paulo, FAPESP, grant numbers #2021/14693-4, #2013/07296-2 and #2017/11986-5; Conselho Nacional de Desenvolvimento Científico e Tecnológico, CNPq, grant number #152607/2022-6, #311769/2022-5 and #406156/2022-0, Financiadora de Estudos e Projetos FINEP #grant number 01.22.0179.00. The authors also thank Shell and the strategic importance of the support given by ANP (Brazil's National Oil, Natural Gas, and Biofuels Agency) through the R&D levy regulation. The authors would like to thank the Brazilian Nanotechnology National Laboratory (LNNano/CNPEM) for the use of XPS facilities (proposal #XPS-20230151).

Supplementary materials

Supplementary material associated with this article can be found, in the online version, at doi:10.1016/j.electacta.2023.143680.

References

[1] B. Yang, W. Ding, H. Zhang, S. Zhang, Recent progress on electrochemical synthesis of ammonia from nitrogen: strategies to improve the catalytic activity and selectivity, Energy Environ. Sci. 14 (2021) 672–687, https://doi.org/10.1039/D0EE02263B.

[2] J.G. Chen, R.M. Crooks, L.C. Seefeldt, K.L. Bren, R.M. Bullock, M.Y. Darensbourg, P.L. Holland, B. Hoffman, M.J. Janik, A.K. Jones, M.G. Kanatzidis, P. King, K. M. Lancaster, S.V. Lymar, P. Pfromm, W.F. Schneider, R.R. Schrock, Beyond fossil fuel-driven nitrogen transformations, Science 360 (2018) eaar6611, https://doi.org/10.1126/science.aar6611.

[3] J.W. Erisman, M.A. Sutton, J. Galloway, Z. Klimont, W. Winiwarter, How a century of ammonia synthesis changed the world, Nat. Geosci. 1 (2008) 636–639, https://doi.org/10.1038/ngeo325.

[4] T. Wu, W. Fan, Y. Zhang, F. Zhang, Electrochemical synthesis of ammonia: progress and challenges, Mater. Today Phys. 16 (2021) 100310, https://doi.org/10.1016/j.mtphys.2020.100310.

[5] L. Wang, M. Xia, H. Wang, K. Huang, C. Qian, C.T. Maravelias, G.A. Ozin, Greening ammonia toward the solar ammonia refinery, Joule 2 (2018) 1055–1074, https://doi.org/10.1016/j.joule.2018.04.017.

[6] S. Wang, F. Ichihara, H. Pang, H. Chen, J. Ye, Nitrogen fixation reaction derived from nanostructured catalytic materials, Adv. Funct. Mater. 28 (2018) 1803309, https://doi.org/10.1002/adfm.201803309.

[7] B.H.R. Suryanto, H.L. Du, D. Wang, J. Chen, A.N. Simonov, D.R. MacFarlane, Challenges and prospects in the catalysis of electroreduction of nitrogen to ammonia, Nat. Catal. 2 (2019) 290–296, https://doi.org/10.1038/s41929-019-0252-4.

[8] L. Shi, Y. Yin, S. Wang, H. Sun, Rational catalyst design for N_2 reduction under ambient conditions: strategies toward enhanced conversion efficiency, ACS Catal. 10 (2020) 6870–6899, https://doi.org/10.1021/acscatal.0c01081.

[9] P. Li, Z. Liu, T. Wu, Y. Zhang, L. Wang, L. Wang, L. Ji, Y. Zhang, Y. Luo, T. Wang, S. Liu, Y. Wu, M. Liu, X. Sun, Ambient electrocatalytic N_2 reduction to NH_3 by metal fluorides, J. Mater. Chem. A 7 (2019) 17761–17765, https://doi.org/10.1039/C9TA04706A.

[10] H. Yang, C. Nan, N. Gao, W. Zhou, F. Gao, D. Dong, D. Dou, Y. Liu, Z. Liang, D. Yang, Three-phase interface of SnO_2 nanoparticles loaded on hydrophobic MoS_2 enhance photoelectrochemical N_2 reduction, Electrochim. Acta 430 (2022) 141086, https://doi.org/10.1016/j.electacta.2022.141086.

[11] Y. Zhang, Y. Wang, X. Mou, C. Song, D. Wang, Engineering oxygen vacancies and low-valent bismuth at the surface of Bi_2MoO_6 nanosheets for boosting electrocatalytic N_2 reduction, Electrochim. Acta 439 (2023) 141661, https://doi.org/10.1016/j.electacta.2022.141661.

[12] X. Zhao, X. Zhang, Z. Xue, W. Chen, Z. Zhou, T. Mu, Fe nanodot-decorated MoS_2 nanosheets on carbon cloth: an efficient and flexible electrode for ambient ammonia synthesis, J. Mater. Chem. A 7 (2019) 27417, https://doi.org/10.1039/C9TA09264A.

[13] H. Zhu, X. Ren, X. Yang, X. Liang, A. Liu, G. Wu, Fe-based catalysts for nitrogen reduction toward ammonia electrosynthesis under ambient conditions, SusMat 2 (2022) 214–242, https://doi.org/10.1002/sus2.70.

[14] G. Tranchida, R.G. Milazzo, M. Leonardi, S. Scalese, L. Pulvirenti, G.G. Condorelli, C. Bongiorno, S. Lombardo, S.M.S. Privitera, Strategies to improve the catalytic activity of Fe-based catalysts for nitrogen reduction reaction, Int. J. Hydrog. Energy (2023), https://doi.org/10.1016/j.ijhydene.2023.03.241.

[15] M. Yang, X. Wang, C.J. Gómez-García, Z. Jin, J. Xin, X. Cao, H. Ma, H. Pang, L. Tan, G. Yang, Y. Kan, Efficient electron transfer from an electron-reservoir polyoxometalate to dual-metal-site metal-organic frameworks for highly efficient electroreduction of nitrogen, Adv. Funct. Mater. 33 (2023) 2214495, https://doi.org/10.1002/adfm.202214495.

[16] S. Chen, X. Liu, J. Xiong, L. Mi, Y. Li, Engineering strategies for boosting the nitrogen reduction reaction performance of MoS_2-based electrocatalysts, Mater. Today Nano 18 (2022) 100202, https://doi.org/10.1016/j.mtnano.2022.100202.

[17] M. Arif, M. Babar, U. Azhar, M. Sagir, M.B. Tahir, M.A. Mushtaq, G. Yasin, M. Mubashir, J.W.R. Chong, K.S. Khoo, P.L. Show, Rational design and modulation strategies of Mo-based electrocatalysts and photo/electrocatalysts towards nitrogen reduction to ammonia (NH_3), J. Chem. Eng. 451 (2023) 138320, https://doi.org/10.1016/j.cej.2022.138320.

[18] X. Chen, C. Ma, Z. Tan, X. Wang, X. Qian, X. Zhang, J. Tian, S. Yan, M. Shao, One-dimensional screw-like MoS_2 with oxygen partially replacing sulfur as an electrocatalyst for the N_2 reduction reaction, Chem. Eng. J. 433 (2022) 134504, https://doi.org/10.1016/j.cej.2022.134504.

[19] L.M. Azofra, C. Sun, L. Cavallo, D.R. MacFarlane, Feasibility of N_2 binding and reduction to ammonia on Fe deposited MoS_2 2D sheets: a DFT study, Chem. Eur. J. 23 (2017) 1–6, https://doi.org/10.1002/chem.201701113.

[20] X. Xu, X. Liu, J. Zhao, D. Wu, Y. Du, T. Yan, N. Zhang, X. Ren, Q. Wei, Interface engineering of MoS_2@$Fe(OH)_3$ nanoarray heterostructure: electrodeposition of MoS_2@$Fe(OH)_3$ as N_2 and H+ channels for artificial NH_3 synthesis under mild conditions, J. Colloid Interface Sci. 606 (2022) 1374–1379, https://doi.org/10.1016/j.jcis.2021.08.099.

[21] C. Ma, D. Liu, Y. Zhang, J.Y. Lee, J. Tian, B. Liu, S. Yan, MOF-derived Fe_2O_3@MoS_2: an efficient electrocatalyst for ammonia synthesis under mild conditions, Chem. Eng. J. 430 (2022) 132694, https://doi.org/10.1016/j.cej.2021.132694.

[22] Y.H. Moon, N.Y. Kim, S.M. Kim, Y.J. Jang, Recent advances in electrochemical nitrogen reduction reaction to ammonia from the catalyst to the system, Catalysts 12 (2022) 1015, https://doi.org/10.3390/catal12091015.

[23] K.C. Pham, Y.H. Chang, D.S. McPhail, C. Mattevi, A.T.S. Wee, D.H.C. Chua, Amorphous molybdenum sulfide on graphene–carbon nanotube hybrids as highly active hydrogen evolution reaction catalysts, ACS Appl. Mater. Interfaces 8 (2016) 5961, https://doi.org/10.1021/acsami.5b09690.

[24] O. Mabayoje, Y. Liu, M. Wang, A. Shoola, A.M. Ebrahim, A.I. Frenkel, C.B. Mullins, Electrodeposition of MoS_x hydrogen evolution catalysts from sulfur-rich precursors, ACS Appl. Mater. Interfaces 11 (2019) 32879–32886, https://doi.org/10.1021/acsami.9b07277.

[25] S.C. Lee, J.D. Benck, C. Tsai, J. Park, A.L. Koh, F. Abild- Pedersen, T.F. Jaramillo, R. Sinclair, Chemical and phase evolution of amorphous molybdenum sulfide catalysts for electrochemical hydrogen production, ACS Nano 10 (2016) 624–632, https://doi.org/10.1021/acsnano.5b05652.

[26] L. Wang, C. Lee, P. Schmuki, Solar water splitting: preserving the beneficial small feature size in porous α-Fe_2O_3 photoelectrodes during annealing, J. Mater. Chem. A 1 (2013) 212–215, https://doi.org/10.1039/C2TA00431C.

[27] A.L. Woodley, C.F. Drury, W.D. Reynolds, W. Calder, X.M. Yang, T.O. Oloya, Improved acid trap methodology for determining ammonia volatilization in wind tunnel experiments, Can. J. Soil Sci. 98 (2018) 193–199, https://doi.org/10.1139/cjss-2017-0081.

[28] D. Liu, G. Zhang, Q. Ji, Y. Zhang, J. Li, Synergistic electrocatalytic nitrogen reduction enabled by confinement of nanosized Au particles onto a two-dimensional Ti_3C_2 substrate, ACS Appl. Mater. Interfaces 11 (2019) 25758–25765, https://doi.org/10.1021/acsami.9b02511.

[29] S.Z. Andersen, V. Colic, S. Yang, J.A Schwalbe, A.C. Nielander, J.M. McEnaney, K. Enemark-Rasmussen, J.G. Baker, A.R. Singh, B.A. Rohr, M.J. Statt, S.J. Blair, S. Mezzavilla, J. Kibsgaard, P.C.K. Vesborg, M. Cargnello, S.F Bent, T.F Jaramillo, I. E.L Stephens, J.K. Norskov, I. Chorkendorff, Nature 570 (2019) 504–508, https://doi.org/10.1038/s41586-019-1260-x.

[30] T. Wu, P. Li, H. Wang, R. Zhao, Q. Zhou, W. Kong, M. Liu, Y. Zhang, X. Sun, F. Gong, Biomass-derived oxygen-doped hollow carbon microtubes for electrocatalytic N_2-to-NH_3 fixation under ambient conditions, Chem. Commun. 55 (2019) 2684–2687, https://doi.org/10.1039/C8CC09867K.

[31] J.F. de Brito, M.B. Costa, K. Rajeshwar, L.H. Mascaro, Ammonia production from nitrogen under simulated solar irradiation, low overpotential, and mild conditions, Electrochim. Acta 421 (2022) 140475, https://doi.org/10.1016/j.electacta.2022.140475.

[32] J. Si, R. Ma, Y. Wu, Y. Dong, K. Yao, Microstructure and magnetic properties of novel powder cores composed of iron-based amorphous alloy and PTFE, J. Mater. Sci. 57 (2022) 8154–8166, https://doi.org/10.1007/s10853-022-07199-4.

[33] H. Sun, X. Ji, Y. Qiu, Y. Zhang, Z. Ma, G.G. Gao, P. Hu, Poor crystalline MoS_2 with highly exposed active sites for the improved hydrogen evolution reaction performance, J. Alloys Compd. 777 (2019) 514–523, https://doi.org/10.1016/j.jallcom.2018.10.364.

[34] Y. Deng, L.R.L. Ting, P.H.L. Neo, Y.J. Zhang, A.A. Peterson, B.S. Yeo, Operando Raman spectroscopy of amorphous molybdenum sulfide (MoS_x) during the electrochemical hydrogen evolution reaction: identification of sulfur atoms as catalytically active sites for H^+ reduction, ACS Catal. 6 (2016) 7790–7798, https://doi.org/10.1021/acscatal.6b01848.

[35] C.G. Morales-Guio, X. Hu, Amorphous molybdenum sulfides as hydrogen evolution catalysts, Acc. Chem. Res. 47 (2014) 2671–2681, https://doi.org/10.1021/ar5002022.

[36] A.J. Mendoza, M.A. Hickner, J. Morgan, K. Rutter, C. Legzdins, Raman spectroscopic mapping of the carbon and PTFE distribution in gas diffusion layers, Fuel Cells 11 (2011) 248–254, https://doi.org/10.1002/fuce.201000096.

[37] J. Zhang, M. Zhao, Y. Zhao, J. Wang, Y. Wu, K. Li, Y. Liu, Microwave-assisted hydrothermal synthesis of Fe-doped 1T/2H-MoS_2 few-layer nanosheets for efficient electromagnetic wave absorbing, J. Alloys Compd. 947 (2023) 169544, https://doi.org/10.1016/j.jallcom.2023.169544.

[38] R. Murugan, A. Ghule, C. Bhongale, H.J. Chang, Thermo-Raman investigations on structural transformations in hydrated MoO_3, J. Mater. Chem. 10 (2000) 2157–2162, https://doi.org/10.1039/B000811G.

[39] E. Mohammadpour, K. Asadpour-Zeynali, α-Fe_2O_3@MoS_2 nanostructure as an efficient electrochemical catalyst for water oxidation, Microchem. J. 157 (2020) 104939, https://doi.org/10.1016/j.microc.2020.104939.

[40] Y. Cha, Y.J. Park, D.H. Kim, Hydrodynamic synthesis of Fe_2O_3@MoS_2 0D/2D nanocomposite material and its application as a catalyst in the glycolysis of polyethylene terephthalate, RSC Adv. 11 (2021) 16841, https://doi.org/10.1039/D1RA02335G.

[41] Z. Yin, J. Zhao, B. Wang, Y. Xu, Z. Li, X. Ma, Insight for the effect of bridging S_2^{2-} in molybdenum sulfide catalysts toward sulfur-resistant methanation, Appl. Surf. Sci. 471 (2019) 670, https://doi.org/10.1016/j.apsusc.2018.12.057.

[42] M. Medina, P.G. Corradini, J.F. de Brito, H.L.S. Santos, L.H. Mascaro, The substrate morphology effect for sulfur-rich amorphous molybdenum sulfide for electrochemical hydrogen evolution reaction, J. Electrochem. Soc. 169 (2022) 026519, https://doi.org/10.1149/1945-7111/ac5067.

[43] A. Jain, M.B. Sadan, A. Ramasubramaniam, Identifying a new pathway for nitrogen reduction reaction on Fe- doped MoS_2 by the coadsorption of hydrogen and N_2, J. Phys. Chem. C 125 (2021) 19980–19990, https://doi.org/10.1021/acs.jpcc.1c04499.

[44] M. Vizza, W. Giurlani, L. Cerri, N. Calisi, A.A. Leonardi, M.J.L. Faro, A. Irrera, E. Berretti, J.V. Perales-Rondón, A. Colina, E.B. Saiz, M. Innocenti, Electrodeposition of molybdenum disulfide (MoS_2) nanoparticles on monocrystalline silicon, Molecules 27 (2022) 5416, https://doi.org/10.3390/molecules27175416.

[45] H. Vrubel, X. Hu, Growth and activation of an amorphous molybdenum sulfide hydrogen evolving catalyst, ACS Catal. 3 (2013) 2002–2011, https://doi.org/10.1021/cs400441u.

[46] S.B. Patil, H.L. Chou, Y.M. Chen, S.H. Hsieh, C.H. Chen, C.C. Chang, S.R. Li, Y. C. Lee, Y.S. Lin, H. Li, Y.J. Chang, Y.H. Lai, D.Y. Wang, Enhanced N_2 affinity of 1T-MoS_2 with a unique pseudo-six-membered ring consisting of N–Li–S– Mo–S–Mo for high ambient ammonia electrosynthesis performance, J. Mater. Chem. A 9 (2021) 1230, https://doi.org/10.1039/D0TA10696H.

[47] G.W. Watt, J.D. Chrisp, *In situ* growth of amorphous $Fe(OH)_3$ on nickel nitrate hydroxide nanoarrays for enhanced electrocatalytic oxygen evolution, ACS Appl. Mater. Interfaces 12 (2020) 12668–12676, https://doi.org/10.1021/acsami.9b19437.

[48] Y. Yuan, N. Fujiwara, S. Tada, R. Kikuchi, An *in situ* DRIFTS study on nitrogen electrochemical reduction over an $Fe/BaZr_{0.8}Y_{0.2}O_{3-\alpha}$-Ru catalyst at 220 °C in an electrolysis cell using a $CsH2PO4/SiP_2O_7$ electrolyte, RSC Adv. 12 (2022) 8474, https://doi.org/10.1039/d2ra00224h.

[49] M. Wang, S. Liu, H. Ji, T. Yang, T. Qian, C. Yan, Salting-out effect promoting highly efficient ambient ammonia synthesis, Nat. Commun. 12 (2021) 3198, https://doi.org/10.1038/s41467-021-23360-0.

[50] H. Zhang, B. Song, W. Zhang, Q. Chen, K. Lu, Y. Cheng, Activation of MoS_2 monolayer electrocatalysts via reduction and phase control in molten sodium for selective hydrogenation of nitrogen to ammonia, Chem. Sci. 13 (2022) 9498, https://doi.org/10.1039/d2sc03804h.

[51] H. Su, L. Chen, Y. Chen, R. Si, Y. Wu, X. Wu, Z. Geng, W. Zhang, J. Zeng, Single atoms of iron on MoS_2 nanosheets for N_2 electroreduction into ammonia, Angew. Chem. Int. Ed. 59 (2020), https://doi.org/10.1002/anie.202009217, 20411e20416.

[52] C. Ma, N. Zhai, B. Liu, S. Yan, Defected MoS_2: an efficient electrochemical nitrogen reduction catalyst under mild conditions, Electrochim. Acta 370 (2021) 137695, https://doi.org/10.1016/j.electacta.2020.137695.

[53] H.Q. Xie, X. Zheng, Q.Y. Feng, X.P. Chen, Z.H. Zou, Q.X. Wang, J. Tang, Y. Li, Y. Ling, Single-step synthesis of Fe−Fe3O4 catalyst for highly efficient and selective electrochemical nitrogen reduction, ChemSusChem 15 (2022) e202200919, https://doi.org/10.1002/cssc.202200919.

[54] Z. Lu, S.E. Saji, J. Langley, Y. Lin, Z. Xie, K. Yang, L. Bao, Y. Sun, S. Zhang, Y.H. Ng, L. Song, N. Cox, Z. Yin, Selective N_2/H_2O adsorption onto 2D amphiphilic amorphous photocatalysts for ambient gas-phase nitrogen fixation, Appl. Catal. B 294 (2021) 120240, https://doi.org/10.1016/j.apcatb.2021.120240.

[55] X. Chen, C. Ma, Z. Tan, X. Wang, X. Qian, X. Zhang, J. Tian, Shihai Yan, M. Shao, One-dimensional screw-like MoS_2 with oxygen partially replacing sulfur as an electrocatalyst for the N_2 reduction reaction, J. Chem. Eng. 433 (2022) 134504, https://doi.org/10.1016/j.cej.2022.134504.

[56] J. Chen, C. Zhang, M. Huang, J. Zhang, J. Zhang, H. Liu, G. Wang, R. Wang, The activation of porous atomic layered MoS_2 basal-plane to induce adjacent Mo atom pairs promoting high efficiency electrochemical N_2 fixation, Appl. Catal. B 285 (2021) 119810, https://doi.org/10.1016/j.apcatb.2020.119810.

[57] B.H.R. Suryanto, D. Wang, L.M. Azofra, M. Harb, L. Cavallo, R. Jalili, D.R. G. Mitchell, M. Chatti, D.R. MacFarlane, MoS_2 polymorphic engineering enhances selectivity in the electrochemical reduction of nitrogen to ammonia, ACS Energy Lett. 4 (2019) 430–435, https://doi.org/10.1021/acsenergylett.8b02257.

[58] J. Li, S. Chen, F. Quan, G. Zhan, F. Jia, Z. Ai, L. Zhang, Accelerated dinitrogen electroreduction to ammonia via interfacial polarization triggered by single-atom protrusion, Chem 6 (2020) 885–901, https://doi.org/10.1016/j.chempr.2020.01.013.

[59] Y. Ma, T. Yang, H. Zou, W. Zang, Z. Kou, L. Mao, Y. Feng, L. Shen, S.J. Pennycook, L. Duan, X. Li, J. Wang, Synergizing Mo single atoms and Mo_2C Nanoparticles on CNTs synchronizes selectivity and activity of electrocatalytic N_2 reduction to ammonia, Adv. Mater. 32 (2020) 2002177, https://doi.org/10.1002/adma.202002177.